Aerospace Science and Technology 124 (2022) 107561

Contents lists available at ScienceDirect

Aerospace Science and Technology

www.elsevier.com/locate/aescte

Modeling and control of a class of urban air mobility tiltrotor aircraft

Weihua Su [a,*], Shen Qu [b], Guoming Zhu [b], Sean Shan-Min Swei [c], Mariko Hashimoto [d], Tao Zeng [e]

[a] Department of Aerospace Engineering and Mechanics, The University of Alabama, Tuscaloosa, AL 35487-0280, United States
[b] Department of Mechanical Engineering, Michigan State University, East Lansing, MI 48824, United States
[c] Department of Aerospace Engineering, Khalifa University, Abu Dhabi, United Arab Emirates
[d] DENSO CORPORATION, Kariya, Aichi, 448-0028, Japan
[e] DENSO International America, Inc., Southfield, MI 48302, United States

ARTICLE INFO

Article history:
Received 2 June 2021
Received in revised form 23 March 2022
Accepted 8 April 2022
Available online 13 April 2022
Communicated by Hever Moncayo

Keywords:
Urban air mobility
Tiltrotor
Flight mechanics
Control

ABSTRACT

This paper aims at developing a control-centric analytical formulation for aeromechanics and flight dynamics of urban air mobility (UAM) vehicles. Such vehicles feature a hybrid configuration with tiltrotors and fixed wings, enabling vertical takeoff/landing capability while attaining level flight range and endurance. A comprehensive nonlinear rigid-body dynamic model is developed by incorporating multiple tiltrotor dynamics and their gyroscopic and inertial coupling effects. A quasi-steady aerodynamic formulation is used to derive the aerodynamic loads on all lifting surfaces. In addition to the conventional control surfaces of the fixed-wing aircraft, the tiltrotor angular positions and rotational speeds are also considered additional control inputs in the derivation of nonlinear flight dynamic equations. These nonlinear equations are then linearized with respect to a set of trimmed conditions to generate the corresponding linear time-invariant state-space models, which are best suited for flight control design. In particular, to capture the critical dynamical behaviors during the transition from vertical to forward flight, the linear models are attained at various angular positions of the tiltrotors. These linear models are then utilized to develop a linear parameter-varying (LPV) model in which the tiltrotor angular position is considered the scheduling parameter. Subsequently, the adaptive model predictive control (MPC) methodology is used to design the flight controllers to achieve a stable and smooth transition flight. The numerical simulations demonstrate the efficacy of the proposed modeling and control approach.

1. Introduction

Urban air mobility (UAM) vehicles have attracted much attention lately from both the aviation industry and the academic community. They are viewed as promising next-generation point-to-point air transportation for urban travel. Though there are still no established standards for UAM vehicles, one key characteristic that is common in most of the proposed UAM vehicles is the vertical takeoff/landing (VTOL) capability enabled by the distributed electric propulsion (DEP) technology [1]. This class of emerging UAM vehicles is known as eVTOL. In particular, a significant subset of such eVTOL vehicles that is adopted by many leading eVTOL manufacturers features a combination of DEP system and fixed wings; for instance, Joby S2/S4, Airbus Vahana, Boeing Phantom Swift, Hyundai/Uber S-A1, and Lilium Jet, to just name a few. This hybrid configuration takes advantage of both cruise flight aerodynamic efficiency of a fixed-wing aircraft and VTOL and hovering capability of a DEP system. Most notably, the mentioned eVTOL vehicles may utilize articulation of thrust vectors to ensure a smooth transition between vertical and forward flights. The thrust vectors can be achieved by either tilting the individual pylon/tiltrotor or rotating the entire fore/aft wing with distributed prop-rotors on each wing. The tiltrotor configuration, while eliminating the need for extra prop-rotors/motors for separate vertical and cruise flight, reduces the vehicle weight and the aerodynamic drag. However, the complexity of tiltrotor dynamics and stable transitioning between vertical and cruise flight utilizing thrust vectoring impose a unique technical challenge. Therefore, developing an analytical and control-centric dynamic model that captures the salient aeromechanics of the transition flight becomes a vitally important research subject [2,3].

* Corresponding author.
E-mail address: suw@eng.ua.edu (W. Su).

https://doi.org/10.1016/j.ast.2022.107561
1270-9638/

Nomenclature

$\mathbf{A}$	state-space system matrix	$\mathbf{S}$	trim cost function
A	rotor disk area ... m^2	T	kinetic energy ... J
a_0, a_1	aerodynamic frames along lifting surface	$\mathcal{T}$	rotor torque ... $N \cdot m$
$\mathbf{B}$	state-space control matrix	U	potential energy ... J
B	body-fixed frame	$\mathbf{u}$	system control input vector
b	local frame	V	volume ... m^3
$\mathbf{C}$	rotational transformation matrix	$\mathbf{v}$	translational velocity ... m/s
C_T	rotor thrust coefficient	W^{ext}	external work ... J
$\mathbf{d}$	rotor mass radial location vector ... m	$\mathbf{x}$	system state vector
$\mathbf{E}$	aerodynamic influence matrices	$\dot{y}$	airfoil velocity component along a_{0y} ... m/s
$\mathcal{F}$	rotor thrust ... N	$\dot{z}$	airfoil velocity component along a_{0z} ... m/s
e	engine frame	$\dot{\alpha}$	airfoil pitch rate ... rad/s
G	global frame	$\boldsymbol{\beta}$	rigid-body velocity vector
$\mathbf{g}$	gravitational acceleration vector ... m/s^2	$\boldsymbol{\Gamma}$	control input of rotor spin angle ... rad
$\mathbf{H}$	angular momentum ... $kg \cdot m^2/s$	$\boldsymbol{\gamma}$	rotor spin angle vector ... rad
$\mathbf{I}$	mass moment of inertia ... $kg \cdot m^2$	δ_e, δ_a, δ_r	deflection of elevator, aileron, and rudder ... rad
$\mathbf{L}$	rotor pylon length vector ... m	$\boldsymbol{\epsilon}_0$	nonlinear equilibrium
$\mathbf{M}_{BB}$, $\mathbf{C}_{BB}$	Inertia and damping matrix of full aircraft	$\boldsymbol{\zeta}$	quaternions
m	mass ... kg	$\boldsymbol{\theta}$	angular position ... rad
N	rotor speed ... rpm	$\boldsymbol{\Xi}$	control input of rotor tilt angle ... rad
$\mathbf{p}$	position vector ... m	$\boldsymbol{\xi}$	rotor tilt angle vector ... rad
$\mathbf{q}$	trim variable	ρ	air density ... kg/m^3
$\mathbf{R}$	load vector	$\boldsymbol{\Omega}_\zeta$	matrix of quaternions differential equation
R	rotor radius ... m	$\boldsymbol{\omega}$	angular velocity ... rad/s
r	rotor frame		

A tiltrotor UAM vehicle is a complex system consisting of rigid and flexible structural components. The aeromechanics and flight dynamics of tiltrotor vehicles couples with unsteady aerodynamics. It results in a highly nonlinear, non-periodic dynamic system that is difficult to analyze and simulate [4]. Tugnoli et al. [5] applied a vortex-particle-based method to calculate the wing and rotor's aerodynamic loads of Vahana eVTOL aircraft (by A^3 and Airbus). Higgins et al. [6] performed an acoustic study on a tilt-wing eVTOL aircraft with distributed propulsion. In rotary-wing aircraft studies, a systematic multi-body dynamic simulation approach [7–12] is usually applied to accurately model all the essential structural components, including the rotors and rigid body vehicle. More recent studies on tiltrotor dynamics include advanced trimming analysis by considering coupled tiltrotor aerodynamic interference [13,14], and application of automatic differentiation method in analyzing tiltrotor flight dynamic sensitivity and stability [15]. It is important to note that integrating the DEP system into the UAM vehicles provides the much-needed operational flight robustness with increased safety and reliability, especially for tiltrotor aircraft during the transition flight. In addition, in order to gain flight range and endurance, a fixed-wing platform can be adopted. Therefore, this paper aims to study a class of hybrid eVTOL vehicles that features a fixed-wing aircraft configured with six tiltrotors DEP systems. There already exist comprehensive rotorcraft analysis tools in the literature and commercial market, such as CAMRAD II [8,9] and RCAS [12]. These packages feature nonlinear aeromechanics formulations with flexible rotor blades and unsteady aerodynamics. They can be applied to study and develop the flight dynamics and control for UAM aircraft. However, from the control point of view, it is critical to develop a comprehensive control-centric vehicle model based on the fundamental principles of different disciplines of tiltrotor aircraft. While some simplifications are inevitable, the salient feature of the proposed flight dynamic model is that it encompasses the complicated aeromechanics and coupled flight dynamics so as to provide a comprehensive mathematical framework that can be used to study the flight characteristics of the proposed UAM vehicles at various flight conditions. In addition, when coupled with motor dynamics and onboard energy management system, the proposed mathematical model will facilitate a more holistic approach to study UAM vehicle flight performance, including minimizing (battery) energy consumption subject to specific flight missions. Moreover, another advantage of the proposed model is that it can readily enable further enhancements to include the analysis of, for example, wing flexibility and aeroelasticity, interaction of rotor/wing aerodynamics, etc. These topics will be the subject of future research.

With the developed model, a comprehensive trim analysis is performed in this paper for the nonlinear dynamic model with respect to the two critical flight scenarios: vertical takeoff flight and transition flight. For the analysis of vertical takeoff, the fixed wing's aerodynamic loads are set to zero, and only the tiltrotor rotational speed is considered the trim variable. In this case, all six tiltrotors are in the upright position. The trim solution is to seek the minimum rotational speed for each of the six rotors while subjecting to a constraint on vertical acceleration to ensure ride quality. For the study of the vehicle's transition from vertical to forward flight, the nonlinear model is linearized at various designated angular positions of the tiltrotor. During the transition flight, only two tiltrotors are commanded to tilt from the vertical position (90°) to the horizontal position (0°), the remaining four tiltrotors are maintained in the vertical position to provide the required lift force, especially at the beginning of transition when forward speed is low. During this quasi-steady process, the vehicle pitch angle, ruddervator deflection angle, as well as the tiltrotor angular position and its rotational speed are considered the trim variables. During the transition, the vehicle's forward flight speed is expected to gradually increase from 0 to a designated cruise speed while maintaining (at least) the hovering altitude. Therefore, once the vehicle picks up the forward flight speed, the four upright tiltrotors' rotational speed can be tuned down according to the increased aerodynamic lift generated by the fixed wing. Eventually, their speeds can be reduced to zero when the vehicle completely transits into a steady and level flight.

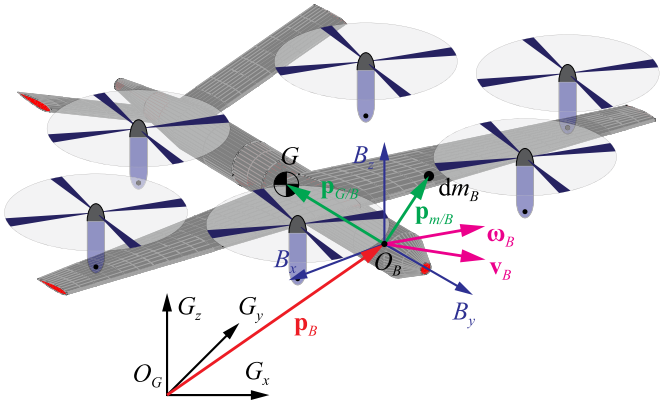

Fig. 1. Global and body reference frames of a rigid-body tiltrotor aircraft (connections between rotors and aircraft are not shown).

The proposed trim analyses generate a collection of linear state-space models representing vertical flight and transition flights at different tiltrotor angular positions. More specifically, these linear models can be used to develop linear parameter-varying (LPV) based controllers [16,17] to assess the stability and performance of the transition flight. For this purpose, the discrete-time adaptive model predictive control (MPC) methodology [18–21] is utilized to formulate the transition flight control problem as a finite-horizon constrained LPV optimal control problem. The standard numerical quadratic programming (QP) technique [22] can be used to attain the real-time flight control strategy.

This paper is organized as follows. Section 2 introduces a nonlinear flight dynamic formulation for tiltrotor aircraft, followed by a numerical model verification for the developed nonlinear dynamics model in Sec. 3. Section 4 presents the linearization of the nonlinear model yielding a control-centric linear state-space representation. The trim analysis for tiltrotor aircraft at vertical takeoff and steady-level/constant-speed climbing flights are also formulated in this section, which is then used in Sec. 5 to numerically study the trim analysis for the transition flight. In Sec. 6, an LPV-based adaptive MPC approach is introduced and used to design an optimal flight controller for transition flight. Finally, conclusions and future works are summarized in Sec. 7.

2. Theoretical formulation

2.1. Rigid-body dynamics and tiltrotor kinematics

In this study, a hybrid UAM aircraft configured with a fixed wing and tiltrotors is considered; see Fig. 1. The dynamic contributions of fixed-wing aircraft and tiltrotors are modeled separately and combined for full vehicle study. First, a body-fixed frame B is defined with respect to the inertial frame G to describe the vehicle's position and orientation; with B_x pointing to the right wing, B_y pointing forward, and B_z completing the right-hand rule. While the B frame can be arbitrarily placed, it is convenient to set the frame's origin O_B within the vehicle's symmetric plane. The inertial position of O_B is represented by $\mathbf{p}_B$, while $\mathbf{p}_{G/B}$ describes the position of the mass center of the fixed-wing aircraft (excluding the tiltrotors) with respect to the B frame. The aircraft's rigid-body velocity is given by

$$\boldsymbol{\beta} = \begin{Bmatrix} \mathbf{v}_B \\ \boldsymbol{\omega}_B \end{Bmatrix} = \begin{Bmatrix} \dot{\mathbf{p}}_B + \boldsymbol{\omega}_B \times \mathbf{p}_B \\ \dot{\boldsymbol{\theta}}_B \end{Bmatrix} \tag{1}$$

where $\mathbf{v}_B$ and $\boldsymbol{\omega}_B$ denote the translational and angular velocities of the rigid body, respectively. Note that all the kinematic quantities are resolved in the B frame.

Fig. 2 illustrates a single tiltrotor on a rigid body. A local frame b with the origin at o_b is established in the aircraft to assess the tiltrotor angular motion, with $\mathbf{p}_b$ denoting the position vector from O_B to o_b. Let $\mathbf{C}^{Bb}$ be the rotational transformation matrix from b frame to B frame. For a rigid-body aircraft, both $\mathbf{p}_b$ and $\mathbf{C}^{Bb}$ are constant upon initialization. The vector $\mathbf{p}_e$, or more specifically $\mathbf{p}_e^b$ as it is resolved relative to the b frame, denotes the constant offset between the b frame and the axis of rotation of the pylon-tiltrotor assembly through o_e. Note that the two vectors $\mathbf{p}_b$ and $\mathbf{p}_e$ can be combined if the aircraft is rigid, however, they are considered separately herein to allow for future development of modeling flexible wing components in the vehicle.

As highlighted in Fig. 2, ξ denotes the 1-D tilt angle of the tiltrotor assembly, which is measured as the rotation of the engine frame e (centered at o_e) about the b_x-axis. The tiltrotor rotation (or spin) angle is denoted by γ, measured as the rotation of the rotor frame r (centered at A) about the e_y-axis, and d is the radial position of an infinitesimal mass dm_r of the rotor. Other than tilting and spinning, the pylon-tiltrotor assembly is considered rigid. The following vectors can be defined according to the reference frames given above,

$$\dot{\xi}^b = \begin{Bmatrix} \dot{\xi} \\ 0 \\ 0 \end{Bmatrix}, \quad \dot{\gamma}^e = \begin{Bmatrix} 0 \\ \dot{\gamma} \\ 0 \end{Bmatrix}, \quad \mathbf{L}^e = \begin{Bmatrix} 0 \\ L \\ 0 \end{Bmatrix}, \quad \text{and} \quad \mathbf{d}^r = \begin{Bmatrix} d \\ 0 \\ 0 \end{Bmatrix}, \tag{2}$$

where the superscripts indicate the reference frames in which the vectors are defined and resolved. For simplicity, the superscripts are omitted in the following equations. The transformation matrices between the local frames are given as follows,

$$\mathbf{C}^{er}(\gamma) = \begin{bmatrix} \cos\gamma & 0 & \sin\gamma \\ 0 & 1 & 0 \\ -\sin\gamma & 0 & \cos\gamma \end{bmatrix}, \quad \mathbf{C}^{be}(\xi) = \begin{bmatrix} 1 & 0 & 0 \\ 0 & \cos\xi & -\sin\xi \\ 0 & \sin\xi & \cos\xi \end{bmatrix}. \tag{3}$$

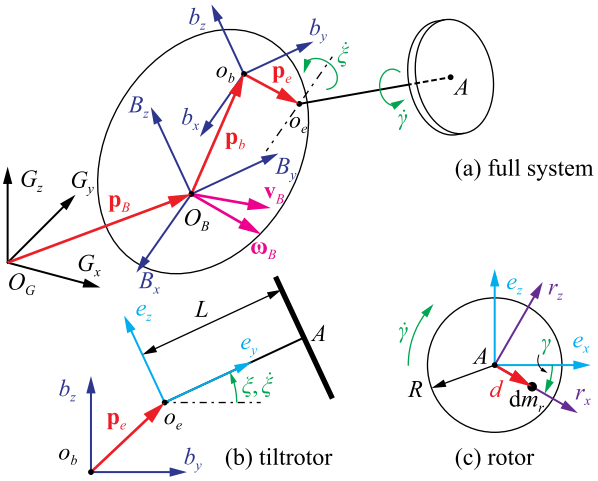

Fig. 2. A free rigid body with a tiltrotor.

Let $\dot{\boldsymbol{\xi}}$ and $\dot{\boldsymbol{\gamma}}$ denote the tilt rate and spin rate vectors, respectively. The rates of these transformation matrices are

$$\begin{aligned}\dot{\mathbf{C}}^{er}(\gamma,\dot{\gamma}) &= \tilde{\dot{\boldsymbol{\gamma}}}\mathbf{C}^{er}(\gamma)\,,\\ \dot{\mathbf{C}}^{be}(\xi,\dot{\xi}) &= \tilde{\dot{\boldsymbol{\xi}}}\mathbf{C}^{be}(\xi)\,,\end{aligned} \tag{4}$$

where the operator $[\tilde{\cdot}]$ refers to a skew-symmetric matrix to complete the cross product of two vectors, i.e., $\mathbf{a}\times\mathbf{b} = [\tilde{\mathbf{a}}]\{\mathbf{b}\} = [\tilde{\mathbf{b}}]^T\{\mathbf{a}\}$. In other words, if $\mathbf{a} = [a_1, a_2, a_3]^T$, then

$$\tilde{\mathbf{a}} = \begin{bmatrix} 0 & -a_3 & a_2 \\ a_3 & 0 & -a_1 \\ -a_2 & a_1 & 0 \end{bmatrix}. \tag{5}$$

Additional rotational transformation matrix between the body and engine frames is given by

$$\mathbf{C}^{Be} = \mathbf{C}^{Bb}\mathbf{C}^{be}\,. \tag{6}$$

The angular velocity and acceleration of the rotor (or the rotor frame r) are given as

$$\begin{aligned}\boldsymbol{\omega}_r &= \boldsymbol{\omega}_B + \mathbf{C}^{Bb}\dot{\boldsymbol{\xi}} + \mathbf{C}^{Bb}\mathbf{C}^{be}(\xi)\dot{\boldsymbol{\gamma}}\,,\\ \dot{\boldsymbol{\omega}}_r &= \dot{\boldsymbol{\omega}}_B + \mathbf{C}^{Bb}\ddot{\boldsymbol{\xi}} + \mathbf{C}^{Bb}\dot{\mathbf{C}}^{be}(\xi)\dot{\boldsymbol{\gamma}} + \mathbf{C}^{Bb}\mathbf{C}^{be}(\xi)\ddot{\boldsymbol{\gamma}}\,,\end{aligned} \tag{7}$$

both are already transformed to the B frame. The position of A, assumed to be the mass center of the rotor, can be described by

$$\begin{aligned}\mathbf{p}_A(\xi) &= \mathbf{p}_B + \mathbf{p}_{A/B}(\xi)\,,\\ \mathbf{p}_{A/B}(\xi) &= \mathbf{p}_b + \mathbf{C}^{Bb}\mathbf{p}_e + \mathbf{C}^{Bb}\mathbf{C}^{be}(\xi)\mathbf{L}\,,\end{aligned} \tag{8}$$

where $\mathbf{p}_{A/B}(\xi)$ denotes the relative position with respect to the B frame. The velocity of point A is obtained by differentiating its position, leading to

$$\mathbf{v}_A = \mathbf{v}_B + \boldsymbol{\omega}_B \times \left(\mathbf{p}_b + \mathbf{C}^{Bb}\mathbf{p}_e + \mathbf{C}^{Bb}\mathbf{C}^{be}\mathbf{L}\right) + \left(\mathbf{C}^{Bb}\dot{\boldsymbol{\xi}}\right) \times \left(\mathbf{C}^{Bb}\mathbf{C}^{be}\mathbf{L}\right). \tag{9}$$

2.2. Energy and external work

The total kinetic energy of the proposed hybrid UAM vehicle is described by

$$T = T_B + T_r\,, \tag{10}$$

where the kinetic energy of the fixed-wing rigid body, T_B, is given by

$$T_B = \frac{1}{2}m_B\left(\mathbf{v}_B\cdot\mathbf{v}_B\right) + m_B\mathbf{v}_B\cdot\left(\boldsymbol{\omega}_B\times\mathbf{p}_{G/B}\right) + \frac{1}{2}\boldsymbol{\omega}_B\cdot\mathbf{H}_B\,, \tag{11}$$

in which m_B is the total mass of the rigid body and $\mathbf{H}_B$ the corresponding angular momentum, which is given by

$$\mathbf{H}_B = \mathbf{I}_B\cdot\boldsymbol{\omega}_B$$

and $\mathbf{I}_B$ denotes the moment of inertia about the B frame. Furthermore, one can refer to Fig. 2 to determine the kinetic energy of the tiltrotors, which is given by

$$T_r = \frac{1}{2} m_r \left(\mathbf{v}_A \cdot \mathbf{v}_A\right) + \frac{1}{2} \boldsymbol{\omega}_r \cdot \mathbf{H}_r \tag{12}$$

in which the rotor's translational and rotational kinetic energy is decoupled since A is considered the mass center of the rotor, and $\mathbf{H}_r$ denotes the angular momentum of the rotor about A, resolved in the B frame, given by

$$\mathbf{H}_r = \mathbf{I}_r \cdot \boldsymbol{\omega}_r \tag{13}$$

where the rotor's inertia $\mathbf{I}_r$ is calculated in the engine frame (e) and then transformed to the body frame (B), and given by

$$\mathbf{I}_r = \mathbf{C}^{Bb} \mathbf{C}^{be} \mathbf{I}_r^e \mathbf{C}^{eb} \mathbf{C}^{bB} . \tag{14}$$

The time derivative of the angular momentum $\mathbf{H}_r$ is given by

$$\frac{\mathrm{d}\mathbf{H}_r}{\mathrm{d}t} = \dot{\mathbf{I}}_r \cdot \boldsymbol{\omega}_r + \mathbf{I}_r \cdot \dot{\boldsymbol{\omega}}_r + \boldsymbol{\omega}_B \times \left(\mathbf{I}_r \cdot \boldsymbol{\omega}_r\right) \tag{15}$$

where the time derivative of rotor inertia is given by

$$\dot{\mathbf{I}}_r = \mathbf{C}^{Bb} \left[\tilde{\dot{\boldsymbol{\xi}}} \mathbf{C}^{be}(\xi) \mathbf{I}_r^e \mathbf{C}^{eb}(\xi) - \mathbf{C}^{be}(\xi) \mathbf{I}_r^e \mathbf{C}^{eb}(\xi) \tilde{\dot{\boldsymbol{\xi}}} \right] \mathbf{C}^{bB} . \tag{16}$$

The potential energy of the complete aircraft comes from the gravity effect, given by

$$U = -m_B \mathbf{g} \cdot \mathbf{p}_B - \left(\mathbf{p}_{G/B} \times m_B \mathbf{g}\right) \cdot \boldsymbol{\theta}_B - m_r \mathbf{g} \cdot \mathbf{p}_B - \left(\mathbf{p}_{A/B} \times m_r \mathbf{g}\right) \cdot \boldsymbol{\theta}_B . \tag{17}$$

The work done by the external loads is

$$W^{\text{ext}} = \mathbf{F}_B^{\text{ext}} \cdot \mathbf{p}_B + \mathbf{M}_B^{\text{ext}} \cdot \boldsymbol{\theta}_B \tag{18}$$

where $\mathbf{F}_B^{\text{ext}}$ and $\mathbf{M}_B^{\text{ext}}$ are the resultant external forces and moments, respectively, applied about the B frame from both the aircraft body and tiltrotor. They include the propulsive and aerodynamic loads, as well as loads due to the deployment of wing control surfaces. The reaction forces/moments between the rigid-body aircraft and tiltrotor are internal loads, hence they do not contribute to the formulation.

2.3. Governing equations of motion

By following the Hamilton's Principle, the governing equation of the complete aircraft is found to be

$$\mathbf{M}_{BB}(\boldsymbol{\xi}) \dot{\boldsymbol{\beta}} + \mathbf{C}_{BB}(\boldsymbol{\beta}, \boldsymbol{\xi}) \boldsymbol{\beta} = \mathbf{R}_B \tag{19}$$

where the inertia and damping matrices and load vector are given by

$$\begin{aligned}
\mathbf{M}_{BB} &= \begin{bmatrix} m_B \mathbf{I}_3 & m_B \tilde{\mathbf{p}}_{G/B}^T \\ m_B \tilde{\mathbf{p}}_{G/B} & \mathbf{I}_B \end{bmatrix} + \begin{bmatrix} m_r \mathbf{I}_3 & m_r \tilde{\mathbf{p}}_{A/B}^T \\ m_r \tilde{\mathbf{p}}_{A/B} & \mathbf{I}_r + m_r \tilde{\mathbf{p}}_{A/B} \tilde{\mathbf{p}}_{A/B}^T \end{bmatrix} \\
\mathbf{C}_{BB} &= \begin{bmatrix} m_B \tilde{\boldsymbol{\omega}}_B & m_B \tilde{\boldsymbol{\omega}}_B \tilde{\mathbf{p}}_{G/B}^T \\ m_B \tilde{\mathbf{p}}_{G/B} \tilde{\boldsymbol{\omega}}_B & \tilde{\boldsymbol{\omega}}_B \mathbf{I}_B \end{bmatrix} + \begin{bmatrix} m_r \tilde{\boldsymbol{\omega}}_B & m_r \tilde{\boldsymbol{\omega}}_B \tilde{\mathbf{p}}_{A/B}^T \\ m_r \tilde{\mathbf{p}}_{A/B} \tilde{\boldsymbol{\omega}}_B & \tilde{\boldsymbol{\omega}}_B \mathbf{I}_r + m_r \tilde{\mathbf{p}}_{A/B} \tilde{\boldsymbol{\omega}}_B \tilde{\mathbf{p}}_{A/B}^T \end{bmatrix} \\
\mathbf{R}_B &= \mathbf{R}^{\text{grav}} + \mathbf{R}^{\text{iner}} + \mathbf{R}^{\text{rate}} + \mathbf{R}^{\text{gyro}} + \mathbf{R}^{\text{ext}}
\end{aligned} \tag{20}$$

in which $\mathbf{I}_3$ denotes the 3-by-3 identity matrix and the gravitational acceleration $\mathbf{g}$ is resolved in the B frame. The term $\mathbf{I}_r + m_r \tilde{\mathbf{p}}_{A/B} \tilde{\mathbf{p}}_{A/B}^T$ in $\mathbf{M}_{BB}$ is nothing but the rotor's mass moment of inertia transferred to the B frame, after applying the Parallel Axis Theorem. In addition, $\mathbf{R}^{\text{grav}}$ denotes the gravity load, $\mathbf{R}^{\text{iner}}$ the inertial load, $\mathbf{R}^{\text{rate}}$ the induced moment due to tiltrotors, $\mathbf{R}^{\text{gyro}}$ the gyroscopic load, and $\mathbf{R}^{\text{ext}}$ the external load, including propulsive and aerodynamic loads.

Equation (19) can be used to solve for the aircraft's dynamic response. However, for easy tracking of propagation of the body frame, additional kinematic equations are established. Given the rigid-body angular velocity $\boldsymbol{\omega}_B = [\omega_{B1}, \omega_{B2}, \omega_{B3}]^T$, one may use the quaternions $\boldsymbol{\zeta} = [\zeta_0, \zeta_1, \zeta_2, \zeta_3]^T$ to describe the rigid-body orientation as follows,

$$\dot{\boldsymbol{\zeta}} = -\frac{1}{2} \boldsymbol{\Omega}_\zeta(\boldsymbol{\beta}) \boldsymbol{\zeta} \tag{21}$$

where

$$\boldsymbol{\Omega}_\zeta(\boldsymbol{\beta}) = \begin{bmatrix} 0 & \omega_{B1} & \omega_{B2} & \omega_{B3} \\ -\omega_{B1} & 0 & -\omega_{B3} & \omega_{B2} \\ -\omega_{B2} & \omega_{B3} & 0 & -\omega_{B1} \\ -\omega_{B3} & -\omega_{B2} & \omega_{B1} & 0 \end{bmatrix} . \tag{22}$$

Note that through a straightforward post-processing effort, the Euler angles can be derived from the quaternions. The rotational transformation matrix $\mathbf{C}^{BG}$ can also be described in terms of the quaternions, i.e.,

$$\mathbf{C}^{BG}(\boldsymbol{\zeta}) = \begin{bmatrix} \zeta_0^2 + \zeta_1^2 - \zeta_2^2 - \zeta_3^2 & 2(\zeta_1\zeta_2 + \zeta_0\zeta_3) & 2(\zeta_1\zeta_3 - \zeta_0\zeta_2) \\ 2(\zeta_1\zeta_2 - \zeta_0\zeta_3) & \zeta_0^2 - \zeta_1^2 + \zeta_2^2 - \zeta_3^2 & 2(\zeta_2\zeta_3 + \zeta_0\zeta_1) \\ 2(\zeta_1\zeta_3 + \zeta_0\zeta_2) & 2(\zeta_2\zeta_3 - \zeta_0\zeta_1) & \zeta_0^2 - \zeta_1^2 - \zeta_2^2 + \zeta_3^2 \end{bmatrix} \tag{23}$$

which leads to the inertial translational velocity of the B frame as

$$\dot{\mathbf{p}}_B^G = \mathbf{C}^{GB}\mathbf{v}_B = \begin{bmatrix}\mathbf{C}^{GB} & \mathbf{0}_3\end{bmatrix}\boldsymbol{\beta} \tag{24}$$

where $\mathbf{C}^{GB} = \left(\mathbf{C}^{BG}\right)^T$. Finally, the combination of Eqs. (19), (21) and (24) completely describes the nonlinear flight dynamical behaviors of the proposed tiltrotor UAM vehicle.

2.4. Inertial and gyroscopic loads

The gravity load vector in Eq. (20) can be described by

$$\mathbf{R}^{\text{grav}} = \begin{Bmatrix}\mathbf{F}^{\text{grav}} \\ \mathbf{M}^{\text{grav}}\end{Bmatrix} = \begin{bmatrix}\mathbf{I}_3 \\ \tilde{\mathbf{p}}_{G/B}\end{bmatrix} m_B\mathbf{g} + \begin{bmatrix}\mathbf{I}_3 \\ \tilde{\mathbf{p}}_{A/B}(\xi)\end{bmatrix} m_r\mathbf{g}. \tag{25}$$

Note that $\mathbf{R}^{\text{iner}}$, $\mathbf{R}^{\text{rate}}$, and $\mathbf{R}^{\text{gyro}}$ in Eq. (20) are all originated from the kinetic energy, and their derivations are presented next.

The tiltrotors are subject to inertial force due to tilting acceleration, centrifugal force, and Coriolis force, and these forces can be described as

$$\mathbf{F}^{\text{iner}} = -m_r\left(\mathbf{C}^{Bb}\left[\ddot{\xi}\times\left(\mathbf{C}^{be}\mathbf{L}\right)\right] + \mathbf{C}^{Bb}\left\{\dot{\xi}\times\left[\dot{\xi}\times\left(\mathbf{C}^{be}\mathbf{L}\right)\right]\right\} + 2\boldsymbol{\omega}_B\times\left\{\mathbf{C}^{Bb}\left[\dot{\xi}\times\left(\mathbf{C}^{be}\mathbf{L}\right)\right]\right\}\right). \tag{26}$$

Additional inertial loads, induced by the rotor angular acceleration, are given by

$$\mathbf{M}^{\text{racc}} = -\mathbf{I}_r\cdot\left(\mathbf{C}^{Bb}\ddot{\xi} + \mathbf{C}^{Bb}\mathbf{C}^{be}\ddot{\gamma}\right), \tag{27}$$

therefore, the equivalent inertial load vector $\mathbf{R}^{\text{iner}}$ can be summarized as

$$\mathbf{R}^{\text{iner}} = \begin{Bmatrix}\mathbf{F}^{\text{iner}} \\ \mathbf{M}^{\text{iner}}\end{Bmatrix} = \begin{bmatrix}\mathbf{I}_3 \\ \tilde{\mathbf{p}}_{A/B}\end{bmatrix}\mathbf{F}^{\text{iner}} + \begin{Bmatrix}\mathbf{0}_{3\times1} \\ \mathbf{M}^{\text{racc}}\end{Bmatrix}. \tag{28}$$

Moreover, the moment of inertia varies with time for a tilting rotor, with its rate of change evaluated in the body frame described in Eq. (16). Such a change of inertia generates a moment, which is given by

$$\mathbf{R}^{\text{rate}} = \begin{Bmatrix}\mathbf{0}_{3\times1} \\ \mathbf{M}^{\text{rate}}\end{Bmatrix} \tag{29}$$

where

$$\mathbf{M}^{\text{rate}} = -\dot{\mathbf{I}}_r\cdot\left(\boldsymbol{\omega}_B + \mathbf{C}^{Bb}\dot{\xi} + \mathbf{C}^{Bb}\mathbf{C}^{be}\dot{\gamma}\right). \tag{30}$$

Finally, the gyroscopic load $\mathbf{R}^{\text{gyro}}$ can be given by

$$\mathbf{R}^{\text{gyro}} = \begin{Bmatrix}\mathbf{0}_{3\times1} \\ \mathbf{M}^{\text{gyro}}\end{Bmatrix} \tag{31}$$

where

$$\mathbf{M}^{\text{gyro}} = -\boldsymbol{\omega}_B\times\left[\mathbf{I}_r\cdot\left(\mathbf{C}^{Bb}\dot{\xi} + \mathbf{C}^{Bb}\mathbf{C}^{be}\dot{\gamma}\right)\right] - \mathbf{I}_r\cdot\left(\mathbf{C}^{Bb}\tilde{\dot{\xi}}\mathbf{C}^{be}\dot{\gamma}\right). \tag{32}$$

2.5. Propulsion

In this study, $\mathbf{R}^{\text{ext}}$ in Eq. (20) includes both propulsive load $\mathbf{R}^{\text{prop}}$ and aerodynamic load $\mathbf{R}^{\text{aero}}$. For simplicity, the static thrust and torque produced by a single rotor are described by

$$\begin{aligned}\mathcal{F} &= C_T\rho A\left(\frac{\pi N}{30}\right)^2 R^2 = C_T\rho A\dot{\gamma}^2R^2 \\ \mathcal{T} &= (-1)^{n-1}C_Q\rho R^5\dot{\gamma}^2,\end{aligned} \tag{33}$$

where C_T and C_Q are the thrust and torque coefficients, respectively, determined by the propeller design, Reynolds number, etc. The formulation is modified from the one provided in Merchant and Miller [23]. Future studies will implement an advanced propulsion model that can provide a more accurate estimation on the thrust and torque during both hover and forward flight. The thrust and torque are aligned along the e_y-axis, whose orientation changes with the angular position of the tiltrotor. Hence, the propulsive load in the body frame B is given by

$$\mathbf{R}^{\text{prop}} = \begin{Bmatrix}\mathbf{F}^{\text{prop}} \\ \mathbf{M}^{\text{prop}}\end{Bmatrix} = \begin{bmatrix}\mathbf{I}_3 \\ \tilde{\mathbf{p}}_{A/B}(\xi)\end{bmatrix}\mathbf{C}^{Be}(\xi)\begin{Bmatrix}0 \\ \mathcal{F} \\ 0\end{Bmatrix} + \begin{bmatrix}\mathbf{0}_3 \\ \mathbf{I}_3\end{bmatrix}\mathbf{C}^{Be}(\xi)\begin{Bmatrix}0 \\ \mathcal{T} \\ 0\end{Bmatrix}. \tag{34}$$

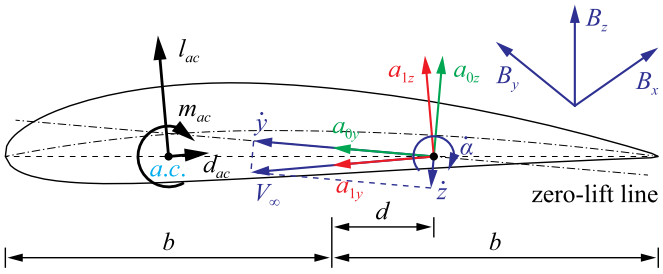

Fig. 3. Aerodynamic frame and load components.

Table 1
Inertial properties of verification model.

	Value	Unit
Body mass, m_B	2280	kg
Body moment of inertia, $\mathbf{I}_{B,xx}$	6400	$\mathrm{kg}\cdot\mathrm{m}^2$
Body moment of inertia, $\mathbf{I}_{B,yy}$	4500	$\mathrm{kg}\cdot\mathrm{m}^2$
Body moment of inertia, $\mathbf{I}_{B,zz}$	9400	$\mathrm{kg}\cdot\mathrm{m}^2$
Rotor mass, m_r	75	kg
Rotor moment of inertia, $\mathbf{I}^e_{r,xx}$	1	$\mathrm{kg}\cdot\mathrm{m}^2$
Rotor moment of inertia, $\mathbf{I}^e_{r,yy}$	2	$\mathrm{kg}\cdot\mathrm{m}^2$
Rotor moment of inertia, $\mathbf{I}^e_{r,zz}$	1	$\mathrm{kg}\cdot\mathrm{m}^2$

2.6. Aerodynamics

The aerodynamic load is calculated at each airfoil section along the span of lifting surfaces. In doing so, the lifting surfaces are meshed with 1-D elements along their span. Referring to Fig. 3, the 2-D quasi-steady aerodynamic loads on each thin airfoil section undergoing arbitrary motions in an incompressible inviscid subsonic flow are described by

$$\begin{aligned} l_{ac} &= \pi\rho b^2\left(-\ddot{z}+\dot{y}\dot{\alpha}-d\ddot{\alpha}\right)+2\pi\rho b\dot{y}^2\left[-\frac{\dot{z}}{\dot{y}}+\left(\frac{1}{2}b-d\right)\frac{\dot{\alpha}}{\dot{y}}\right]+\rho b\dot{y}^2 c_{l\delta}\delta \\ m_{ac} &= \pi\rho b^3\left[\frac{1}{2}\ddot{z}-\dot{y}\dot{\alpha}-\left(\frac{1}{8}b-\frac{1}{2}d\right)\ddot{\alpha}\right]+2\rho b^2\dot{y}^2 c_{m\delta}\delta \\ d_{ac} &= -2\pi\rho b\dot{y}^2\left(-\frac{\dot{z}}{\dot{y}}-d\frac{\dot{\alpha}}{\dot{y}}\right)^2+\rho b\dot{y}^2 c_{d\delta}\delta \end{aligned} \tag{35}$$

where δ is the trailing-edge flap deflection angle, b the semichord, d the distance of midchord in front of the reference axis, $c_{l\delta}$ the lift coefficient, $c_{m\delta}$ the moment coefficient, and $c_{d\delta}$ the drag coefficient. The sectional aerodynamic loads are transformed to the body frame B, given by

$$\begin{aligned} \mathbf{f}^{\text{aero}} &= \mathbf{C}^{Ba_1}\left\{0 \quad d_{ac} \quad l_{ac}\right\}^T, \\ \mathbf{m}^{\text{aero}} &= \mathbf{C}^{Ba_1}\left\{m_{ac}+l_{ac}\left(\tfrac{1}{2}b+d\right) \quad 0 \quad 0\right\}^T. \end{aligned} \tag{36}$$

The distributed aerodynamic force and moment are further integrated to obtain the resultant aerodynamic load about the B frame as follows,

$$\mathbf{R}^{\text{aero}} = \begin{Bmatrix} \mathbf{E}_f\mathbf{f}^{\text{aero}} \\ \mathbf{E}_m\mathbf{m}^{\text{aero}} \end{Bmatrix} \tag{37}$$

where $\mathbf{E}_f$ and $\mathbf{E}_m$ are the influence matrices determined by the numerical integration scheme.

The aerodynamic model implemented in the current work does not consider the unsteadiness and 3D effects, and it does not involve the drag created by the fuselage. Further enhancement with the aerodynamic coupling among the wing, fuselage, and propellers will require a more comprehensive model. The current work aims to establish an analytical flight dynamic model for the class of urban air mobility vehicles so that a robust control algorithm can be explored for such vehicles. Therefore, the simplified model can effectively estimate the aerodynamic loads for the control development.

3. Model verification

In order to verify the nonlinear tiltrotor dynamic model developed in Section 2, we consider a single tiltrotor on a rigid body as illustrated in Fig. 2. For simplicity, the origin of body frame B is at the rigid body's mass center, i.e. $\mathbf{p}_{G/B}=\mathbf{0}$. The pivot point of the tiltrotor, o_e, is chosen to be the same as o_b, O_B, and O_G, i.e., the pivot point is the same as the mass center and B frame origin. The pylon length L is set to 0.5 m. The inertial properties of the rigid body and rotor can be found in Table 1.

The model verification is conducted in Matlab/Simulink environment by utilizing the Simulink Simscape™ Multibody™ toolbox. The verification procedure is described in Fig. 4. Note that the Simscape™ toolbox uses rotor torque as the input, while the developed analytical

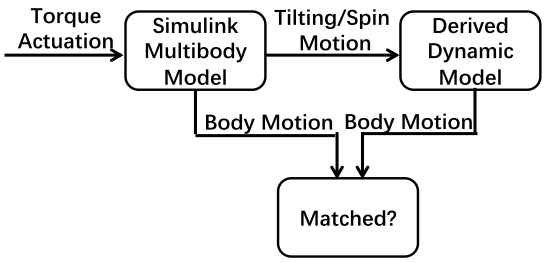

Fig. 4. Tiltrotor flight dynamic model verification process.

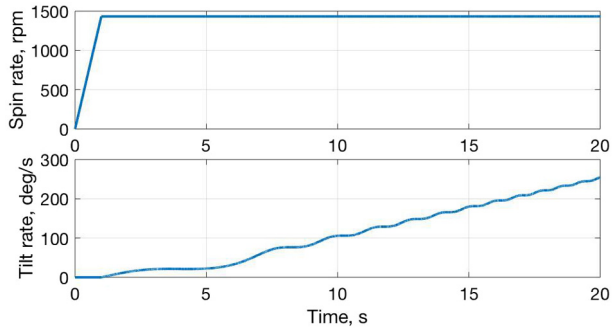

Fig. 5. Rotor rotational speed and tilt angle subject to predefined torques.

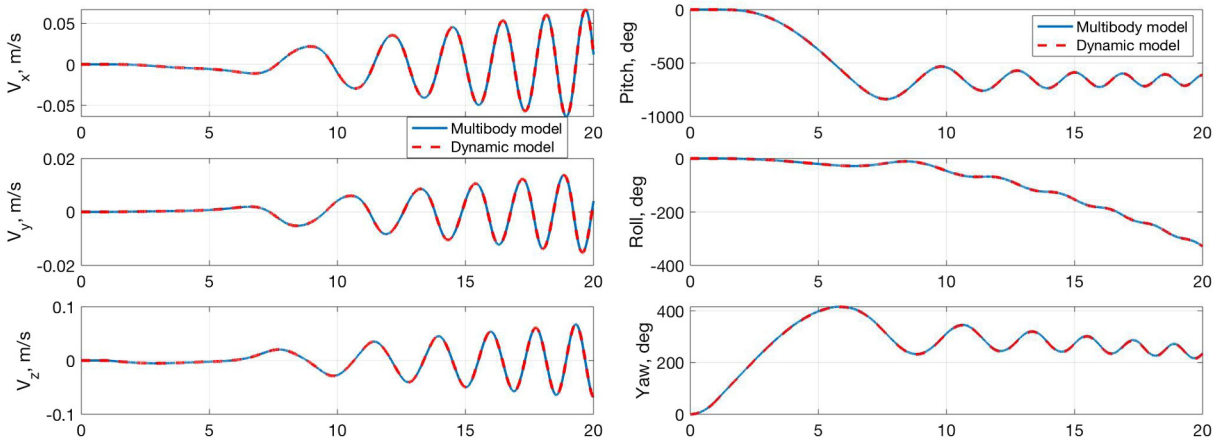

Fig. 6. Model verification: body velocities and Euler angles.

model utilizes rotor kinematics as the input. Therefore, to verify the analytical model, in Simscape™, a predefined torque is applied to the single rotor model to spin the rotor, followed by a predefined torque to tilt the pylon-rotor assembly. The rotor kinematics is recorded in Simscape™ and applied to the analytical model as input. Specifically, from 0 to 1 s, a constant torque of 300 N · m is applied to spin the rotor with initial acceleration, followed by a constant torque of 5 N · m applied to tilt the pylon-rotor assembly from 1 to 20 s. The system is initially set at rest. From the Simscape™ Multibody™ simulations, the resulting rotor spin and tilt motions are shown in Fig. 5, which are then fed into the analytical model as its inputs. Finally, the body linear velocity components and the Euler angles are simulated and compared in Fig. 6. It can be shown that the two responses are matched very well, hence numerically validating the proposed analytical tiltrotor dynamic formulation.

4. Linearization and trim analysis

4.1. Linear state-space equation

In this section, we consider a hybrid UAM vehicle with n number of tiltrotors. To facilitate the linearization process, we define the following control inputs that include both rotor tilt angles and spin kinematics as

$$\begin{aligned} \boldsymbol{\Xi}^T &= \{\xi_1 \quad \cdots \quad \xi_n\} \\ \boldsymbol{\Gamma}^T &= \{\gamma_1 \quad \cdots \quad \gamma_n\}. \end{aligned} \tag{38}$$

The Taylor series expansion is applied to the governing equation with respect to a given equilibrium $\boldsymbol{\epsilon}_0$ with the corresponding control input $\mathbf{u}_0$, in which

$$\begin{aligned}\boldsymbol{\epsilon}_0^T &= \left\{ \boldsymbol{\beta}_0^T \quad \dot{\boldsymbol{\beta}}_0^T \quad \boldsymbol{\zeta}_0^T \quad \dot{\boldsymbol{\zeta}}_0^T \quad \left(\mathbf{p}_{B,0}^G\right)^T \quad \left(\dot{\mathbf{p}}_{B,0}^G\right)^T \right\} \\ \mathbf{u}_0^T &= \left\{ \delta_{e,0}^T \quad \delta_{a,0}^T \quad \delta_{r,0}^T \quad \boldsymbol{\Xi}_0^T \quad \dot{\boldsymbol{\Xi}}_0^T \quad \ddot{\boldsymbol{\Xi}}_0^T \quad \dot{\boldsymbol{\Gamma}}_0^T \quad \ddot{\boldsymbol{\Gamma}}_0^T \right\}\end{aligned} \tag{39}$$

After the expansion, high order terms are neglected, and terms with the same variables are grouped together, leading to the linearized equations of motion as follows,

$$\begin{aligned}&\left(\mathbf{M}_{BB}|_0 - \left.\frac{\partial \mathbf{R}_B}{\partial \dot{\boldsymbol{\beta}}}\right|_0\right)\Delta\dot{\boldsymbol{\beta}} + \left(\mathbf{C}_{BB}|_0 + \left.\frac{\partial \mathbf{C}_{BB}}{\partial \boldsymbol{\beta}}\right|_0 \boldsymbol{\beta}_0 - \left.\frac{\partial \mathbf{R}_B}{\partial \boldsymbol{\beta}}\right|_0\right)\Delta\boldsymbol{\beta} \\ &\qquad = \left.\frac{\partial \mathbf{R}_B}{\partial \boldsymbol{\zeta}}\right|_0 \Delta\boldsymbol{\zeta} + \left.\frac{\partial \mathbf{R}_B}{\partial \delta_e}\right|_0 \Delta\delta_e + \left.\frac{\partial \mathbf{R}_B}{\partial \delta_a}\right|_0 \Delta\delta_a + \left.\frac{\partial \mathbf{R}_B}{\partial \delta_r}\right|_0 \Delta\delta_r \\ &\qquad\quad + \left(\left.\frac{\partial \mathbf{R}_B}{\partial \boldsymbol{\Xi}}\right|_0 - \left.\frac{\partial \mathbf{M}_{BB}}{\partial \boldsymbol{\Xi}}\right|_0 \dot{\boldsymbol{\beta}}_0 - \left.\frac{\partial \mathbf{C}_{BB}}{\partial \boldsymbol{\Xi}}\right|_0 \boldsymbol{\beta}_0\right)\Delta\boldsymbol{\Xi} \\ &\qquad\quad + \left.\frac{\partial \mathbf{R}_B}{\partial \dot{\boldsymbol{\Xi}}}\right|_0 \Delta\dot{\boldsymbol{\Xi}} + \left.\frac{\partial \mathbf{R}_B}{\partial \ddot{\boldsymbol{\Xi}}}\right|_0 \Delta\ddot{\boldsymbol{\Xi}} + \left.\frac{\partial \mathbf{R}_B}{\partial \dot{\boldsymbol{\Gamma}}}\right|_0 \Delta\dot{\boldsymbol{\Gamma}} + \left.\frac{\partial \mathbf{R}_B}{\partial \ddot{\boldsymbol{\Gamma}}}\right|_0 \Delta\ddot{\boldsymbol{\Gamma}} \\ &\Delta\dot{\boldsymbol{\zeta}} = -\frac{1}{2}\left.\frac{\partial \boldsymbol{\Omega}_\zeta(\boldsymbol{\beta})}{\partial \boldsymbol{\beta}}\right|_0 \Delta\boldsymbol{\beta}\boldsymbol{\zeta}_0 - \frac{1}{2}\boldsymbol{\Omega}_\zeta(\boldsymbol{\beta}_0)\Delta\boldsymbol{\zeta} \\ &\Delta\dot{\mathbf{p}}_B^G = \left[\left.\frac{\partial \mathbf{C}^{GB}(\boldsymbol{\zeta})}{\partial \boldsymbol{\zeta}}\right|_0 \Delta\boldsymbol{\zeta} \quad \mathbf{0}_3\right]\boldsymbol{\beta}_0 + \left[\mathbf{C}^{GB}(\boldsymbol{\zeta}_0) \quad \mathbf{0}_3\right]\Delta\boldsymbol{\beta}\end{aligned} \tag{40}$$

where $(\cdot)|_0$ means the corresponding quantity evaluated at the given equilibrium. Furthermore, Eq. (40) can be rewritten in terms of the state-space representation as

$$\dot{\mathbf{x}} = \mathbf{A}\mathbf{x} + \mathbf{B}\mathbf{u} \tag{41}$$

where $\mathbf{x}$ and $\mathbf{u}$ denote the state and control input, respectively, and are defined by

$$\begin{aligned}\mathbf{x}^T &= \left\{ \Delta\boldsymbol{\beta}^T \quad \Delta\boldsymbol{\zeta}^T \quad \Delta\left(\mathbf{p}_B^G\right)^T \right\} \\ \mathbf{u}^T &= \left[\Delta\delta_e^T \quad \Delta\delta_a^T \quad \Delta\delta_r^T \quad \Delta\boldsymbol{\Xi}^T \quad \Delta\dot{\boldsymbol{\Xi}}^T \quad \Delta\ddot{\boldsymbol{\Xi}}^T \quad \Delta\dot{\boldsymbol{\Gamma}}^T \quad \Delta\ddot{\boldsymbol{\Gamma}}^T \right]\end{aligned} \tag{42}$$

and the matrices $\mathbf{A}$ and $\mathbf{B}$ are given by

$$\mathbf{A} = \begin{bmatrix} -\lambda\left(\mathbf{C}_{BB}|_0 + \left.\frac{\partial \mathbf{C}_{BB}}{\partial \boldsymbol{\beta}}\right|_0 \boldsymbol{\beta}_0 - \left.\frac{\partial \mathbf{R}_B}{\partial \boldsymbol{\beta}}\right|_0\right) & \lambda\left.\frac{\partial \mathbf{R}_B}{\partial \boldsymbol{\zeta}}\right|_0 & \mathbf{0}_{6\times 3} \\ -\frac{1}{2}\left.\frac{\partial \boldsymbol{\Omega}_\zeta(\boldsymbol{\beta})}{\partial \boldsymbol{\beta}}\right|_0 \boldsymbol{\zeta}_0 & -\frac{1}{2}\boldsymbol{\Omega}_\zeta(\boldsymbol{\beta}_0) & \mathbf{0}_{4\times 3} \\ \left[\mathbf{C}^{GB}(\boldsymbol{\zeta}_0) \quad \mathbf{0}_3\right] & \left.\frac{\partial \mathbf{C}^{GB}(\boldsymbol{\zeta})}{\partial \boldsymbol{\zeta}}\right|_0 \mathbf{v}_{B_0} & \mathbf{0}_{3\times 3} \end{bmatrix} \tag{43}$$

in which $\lambda = \left(\mathbf{M}_{BB}|_0 - \left.\frac{\partial \mathbf{R}_B}{\partial \dot{\boldsymbol{\beta}}}\right|_0\right)^{-1}$, and $\mathbf{B} = \lambda\left[\mathbf{B}_R \quad \mathbf{B}_T\right]$, where

$$\begin{aligned}\mathbf{B}_R &= \begin{bmatrix} \left.\frac{\partial \mathbf{R}_B}{\partial \delta_e}\right|_0 & \left.\frac{\partial \mathbf{R}_B}{\partial \delta_a}\right|_0 & \left.\frac{\partial \mathbf{R}_B}{\partial \delta_r}\right|_0 \\ 0 & 0 & 0 \\ 0 & 0 & 0 \end{bmatrix} \\ \mathbf{B}_T &= \begin{bmatrix} \left(\left.\frac{\partial \mathbf{R}_B}{\partial \boldsymbol{\Xi}}\right|_0 - \left.\frac{\partial \mathbf{M}_{BB}}{\partial \boldsymbol{\Xi}}\right|_0 \dot{\boldsymbol{\beta}}_0 - \left.\frac{\partial \mathbf{C}_{BB}}{\partial \boldsymbol{\Xi}}\right|_0 \boldsymbol{\beta}_0\right) & \left.\frac{\partial \mathbf{R}_B}{\partial \dot{\boldsymbol{\Xi}}}\right|_0 & \left.\frac{\partial \mathbf{R}_B}{\partial \ddot{\boldsymbol{\Xi}}}\right|_0 & \left.\frac{\partial \mathbf{R}_B}{\partial \dot{\boldsymbol{\Gamma}}}\right|_0 & \left.\frac{\partial \mathbf{R}_B}{\partial \ddot{\boldsymbol{\Gamma}}}\right|_0 \\ 0 & 0 & 0 & 0 & 0 \\ 0 & 0 & 0 & 0 & 0 \end{bmatrix}.\end{aligned} \tag{44}$$

4.2. Trim solutions

Two types of trim problems are considered in this study. The first is to trim for a steady longitudinal flight with a constant speed; including both steady-level flight and constant climbing, in which the equilibrium equation can be obtained by setting $\mathbf{R}_B = 0$ in Eq. (19). Only three components within the equilibrium equation need to be satisfied in these flight scenarios. Therefore, the cost function can be defined as

$$\mathbf{S}^T = \left\{ \mathbf{R}_{B,2} \quad \mathbf{R}_{B,3} \quad \mathbf{R}_{B,4} \right\} \tag{45}$$

and the trim variables are

$$\mathbf{q}^T = \left\{ \alpha_B \quad \delta_e \quad N \right\} \tag{46}$$

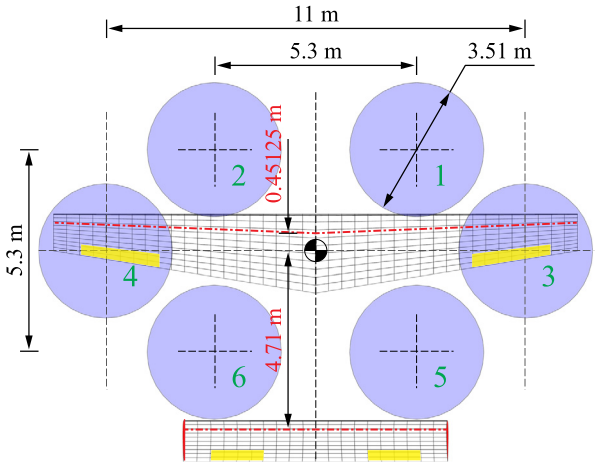

Fig. 7. Geometry of proposed tiltrotor UAM aircraft (top view).

where the body incidence angle α_B is equal to the pitch angle. The solution starts from an initial guess of the trim variable $\mathbf{q}_0$. The Newton-Raphson method is used to search for the solution of $\mathbf{q}$ that satisfies $\mathbf{S}(\mathbf{q}) = 0$. At each step, the search direction is determined by

$$\begin{aligned} \Delta\mathbf{q}_i &= -\left(\frac{\partial \mathbf{S}}{\partial \mathbf{q}}\right)_i^{-1} \mathbf{S}_i \\ \mathbf{q}_{i+1} &= \mathbf{q}_i + \Delta\mathbf{q}_i \end{aligned} \tag{47}$$

in which the Jacobian matrix $\dfrac{\partial \mathbf{S}}{\partial \mathbf{q}}$ is evaluated at each step i using the finite difference method. The search continues until a user-defined tolerance $\varepsilon_{\text{trim}}$ is satisfied, i.e.,

$$\|\mathbf{S}(\mathbf{q})\|_2 \leq \varepsilon_{\text{trim}} . \tag{48}$$

The second trim problem is to find the required rotor speed during the vertical takeoff. In this scenario, the fixed-wing aerodynamics does not participate in the solution, and the body incidence angle is reasonably small to be set to zero. Therefore, in this case, the trim variable consists of rotor speeds only, i.e.,

$$\mathbf{q}^T = \begin{Bmatrix} N_1 & N_2 & \cdots & N_n \end{Bmatrix} . \tag{49}$$

The cost function for trimmed vertical flight becomes

$$\mathbf{S}^T = \begin{Bmatrix} \mathbf{R}_{B,3} - (m_B + m_r)\,\mathbf{a}_z & \mathbf{R}_{B,4} & \mathbf{R}_{B,5} & \mathbf{R}_{B,6} \end{Bmatrix} \tag{50}$$

where $\mathbf{a}_z$ is the constrained vertical acceleration during takeoff, to ensure the compliance with the ride quality requirement. The approach to trim for the vertical flight is the same as level flight. However, the Jacobian matrix is usually not square as the number of rotors used for trim might be greater than four. In this case, the Moore-Penrose pseudo-inverse of the Jacobian is used to search for feasible trim solutions. In general, the solution is not unique; however, the preferred solution should result in the minimum infinity-norm of $\mathbf{q}$ ($\min \|\mathbf{q}\|_\infty$), which corresponds to the lowest possible peak rotor speed. If any rotor malfunctions, the corresponding rotor speed can be set to zero or reduced to a specific value. It is then removed from the list of trim variables in Eq. (49) during the search.

5. Trim analysis

Fig. 7 shows the top view of an urban air mobility aircraft model of interest that is based on the vehicle platform Fig. 1, with six rotors at 90° orientation and the fuselage not shown. The dashed-dotted line indicates the reference line of lifting surfaces, which is 25% the chord from the leading edge. Both the main wing and v-tail are modeled as rigid lifting surfaces. Table 2 lists the inertial parameters of the fixed-wing aircraft and rotor, and Table 3 lists the aerodynamic parameters of the main wing and v-tail. The main wing contains an aileron, as indicated in Fig. 7, which occupies 25% of the chord and extends from 60% to 90% of the wing span. A ruddervator is defined on the v-tail, occupying 25% of the chord, and from 40% to 80% of the tail span. The propulsive coefficients are estimated based on the rotor disk dimension and the flight condition; they are $C_T = 1.0 \times 10^{-2}$ and $C_Q = 6.3 \times 10^{-4}$.

5.1. Trimming for vertical takeoff

Fig. 8 shows the trimmed rotor speed and thrust force during vertical takeoff if all six rotors operate at nominal conditions, in which all rotors have the same speed and thrust. This figure can be used to find the required rotor speed and thrust during the initial vertical takeoff acceleration and the continuing vertical flight at a constant speed. Since only the static thrust is considered in this study, the trim solution turns out to be independent of the takeoff speed.

In addition, we also study important scenarios where one rotor fails to be functional during the takeoff. For this purpose, we first assume that rotor 1 (refer to Fig. 7) is malfunctioning. When this happens, rotor 1's speed is set to zero; hence no thrust is generated

Table 2
Inertial properties of UAM aircraft.

	Value	Unit
Body mass, m_B	2240.73	kg
Body moment of inertia, $\mathbf{I}_{B,xx}$	12000	$\text{kg} \cdot \text{m}^2$
Body moment of inertia, $\mathbf{I}_{B,yy}$	9400	$\text{kg} \cdot \text{m}^2$
Body moment of inertia, $\mathbf{I}_{B,zz}$	20000	$\text{kg} \cdot \text{m}^2$
Rotor mass, m_r	4.55	kg
Rotor moment of inertia, $\mathbf{I}^e_{r,xx}$	3.5	$\text{kg} \cdot \text{m}^2$
Rotor moment of inertia, $\mathbf{I}^e_{r,yy}$	7.0	$\text{kg} \cdot \text{m}^2$
Rotor moment of inertia, $\mathbf{I}^e_{r,zz}$	3.5	$\text{kg} \cdot \text{m}^2$

Table 3
Aerodynamic properties of wing and v-tail of UAM aircraft.

	Wing	Tail	Unit
Airfoil	NACA 0012	NACA 0012	–
Ref. axis location (from L.E.)	25%	25%	–
Span	13.720	6.900	m
Sweep angle	−2.306	0	°
Dihedral angle	0	0	°
Chord (root/tip)	2.075/0.970	1.080/1.080	m
Incidence angle (no twist)	3.1598	1.0626	°

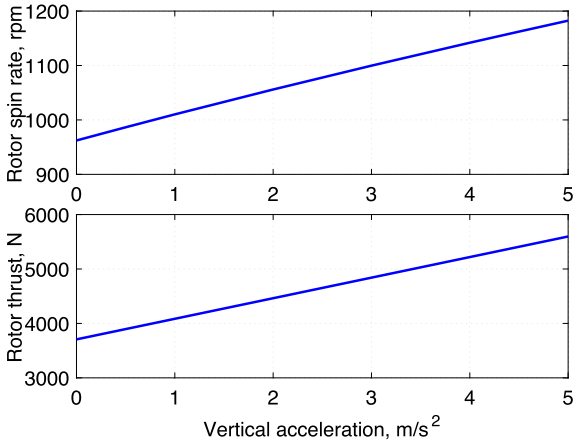

Fig. 8. Rotor spin rate and thrust during nominal vertical takeoff (identical spin rate and thrust for all rotors).

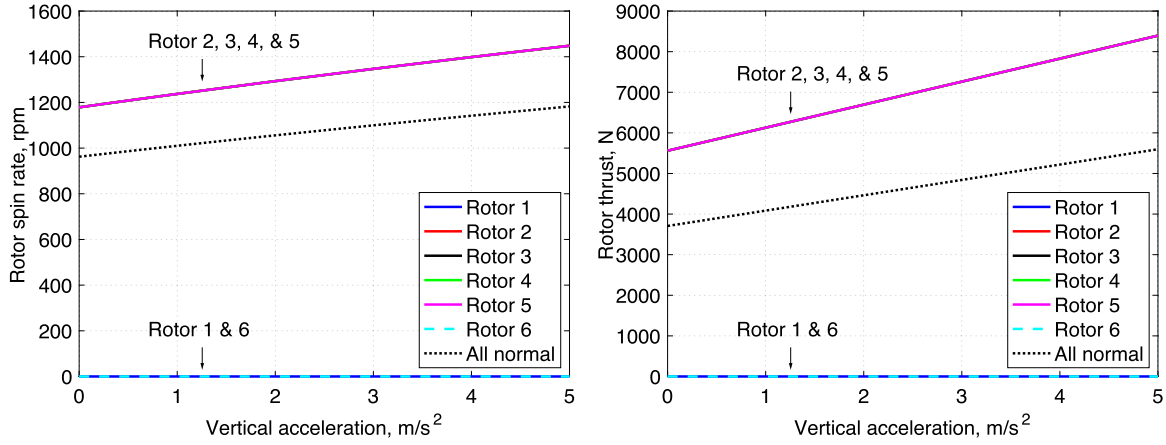

Fig. 9. Individual rotor spin rate and thrust when rotor 1 fails. (For interpretation of the colors in the figure(s), the reader is referred to the web version of this article.)

from that rotor. For the vehicle to continue its vertical flight at the required acceleration, the remaining rotors must be commanded to adjust their speeds, so the output thrusts are re-distributed to maintain the vertical flight. Fig. 9 shows the re-distributed rotor speeds and thrusts. As can be seen, to balance the thrust-induced moment, the speed of rotor 6 is also reduced to zero. In contrast, the remaining four rotors are sped up by about 23%, resulting in about 50% increase in individual thrust. Note that the total thrust remains the same as required by the trimmed flight. We also consider the case when rotor 3 malfunctions. The corresponding trim results are shown in Fig. 10.

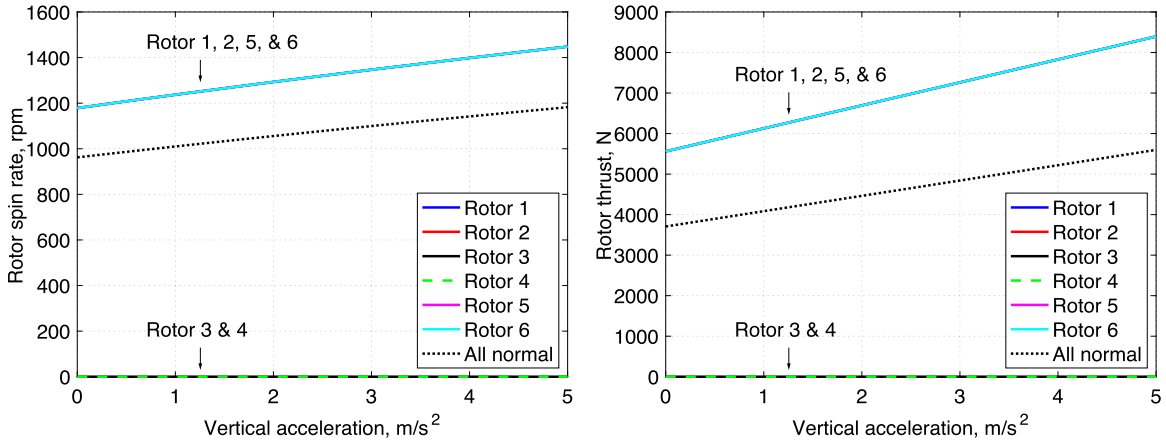

Fig. 10. Individual rotor spin rate and thrust when rotor 3 fails.

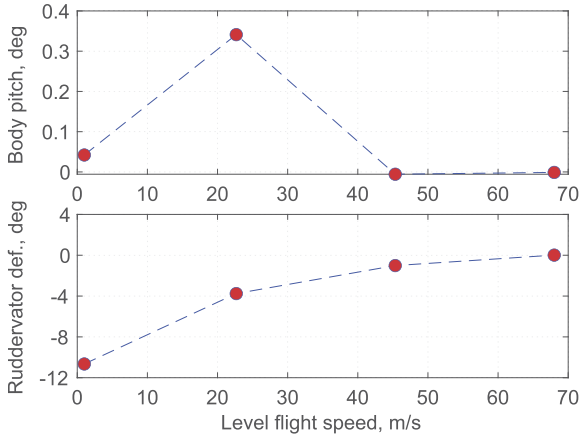

Fig. 11. Trimmed aircraft body pitch and ruddervator deflection during transition flight.

In this case, the speed of rotor 4 is set to zero, and the results in Fig. 10 show the same quantitative change in rotor outputs in order to maintain the vertical flight.

5.2. Trimming for transition flight

In this study, we focus on the forward transition flight after the aircraft has reached its full altitude of 304.8 m at the end of vertical flight. For simplicity, this transition is assumed to be a quasi-steady trimmed process as rotors tilt from vertical position (90°) to horizontal position (0°). Only the middle two tiltrotors (3 and 4, refer to Fig. 7) are commanded to tilt, as these two rotors are sufficient to provide the necessary thrust for the forward flight when they are in the horizontal position. The remaining vertical rotors provide sufficient lifting capability during the transition, as evidenced by the failure analysis presented earlier when both tiltrotors 3 and 4 are absent during vertical flight. To attain the trimmed models for transition flight, we consider the four tilt angular positions of interest, namely, $[90°, 60°, 30°, 0°]$. In other words, between vertical flight and level cruise flight, we add two transient flight conditions, where rotors 3 and 4 are prescribed with a tilt angle of 60° and 30°, respectively. The trim solutions during the transition can then be found using the formulation discussed in Sec. 4.2. It should be noted that during the transition flight, the aircraft forward flight speed is expected to increase from zero to full level flight speed of 68 m/s. Therefore, the lift generated by the fixed wing will gradually increase as the aircraft gains forward velocity. Consequently, the rotational speeds of those four vertical rotors can gradually reduce to zero at the end of the transition.

In this trim analysis, the trim variables are the body pitch angle and ruddervator deflection angle, along with rotor tilt angle and rotor spin rate. Fig. 11 shows the aircraft body pitch angle and ruddervator deflection during transition flight, whereas Figs. 12 and 13 show the rotor tilt angles and spin rates. Because the rotor kinematics is symmetric during the transition, hence those rotors not shown in Figs. 12 and 13 should take negative values. Note that the spin rates of those vertical rotors are specified to yield a small body pitch angle from the trim analysis. This small body pitch angle ensures the ride quality while transitioning from vertical flight to forward flight. Further optimization study can also be carried out to include the rotor kinematics with minimum power consumption during the transition.

6. Transition flight control design

One of the main objectives of the trim studies presented in Sec. 4 is to generate a set of linear state-space dynamic models that are best suited for flight control design. In particular, in this section, we focus on developing the robust and optimal stabilizing controllers for the proposed class of hybrid tiltrotor UAM vehicles during transition flight. Recall that only tiltrotors 3 and 4 (refer to Fig. 7) are

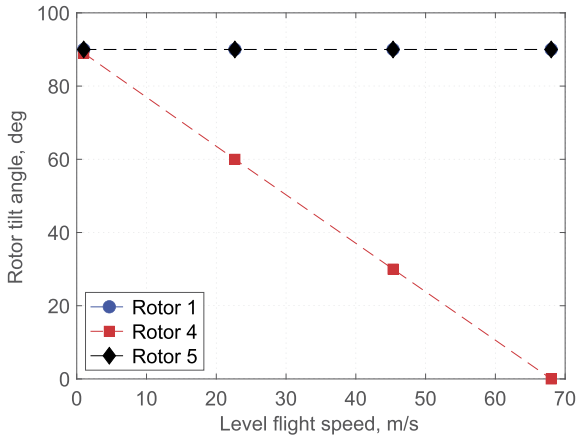

Fig. 12. Trimmed rotor tilt angle during transition flight.

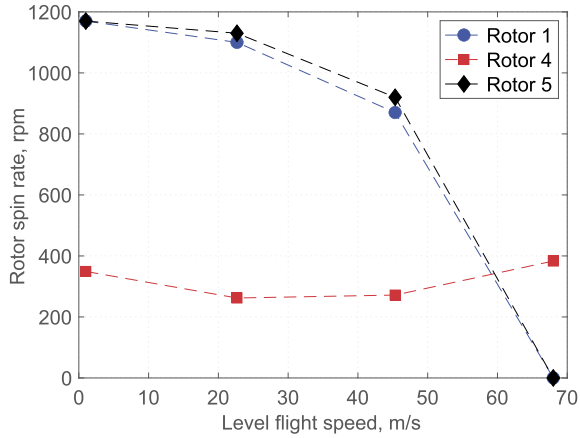

Fig. 13. Trimmed rotor spin rate during transition flight.

commanded to tilt during the transition. By following the quasi-steady process presented earlier, a set of trimmed models can be obtained at chosen rotor tilt angles of $[90°, 60°, 30°, 0°]$. Given these four trimmed models, we can then develop a linear parameter-varying (LPV) model, in which the rotor tilt angle is considered the scheduling parameter. Subsequently, an adaptive model predictive controller (MPC) [18–20] can be designed for the developed LPV model to achieve stable transition flight with guaranteed performance.

6.1. LPV modeling and adaptive MPC

An LPV model is a linear time-invariant (LTI) state-space model in which the system matrices are an affine function of (time-varying) parameters, known as scheduling parameters. As being mentioned, in this study, the scheduling parameter is the rotor tilt angle. Using the interpretation method proposed in [16], a discrete-time LPV system model can be given by

$$\begin{cases} x(k+1) = A(\rho)x(k) + B(\rho)u(k) \\ \quad y(k) = C(\rho)x(k)\,, \quad k = 0, 1, 2, \ldots \end{cases} \tag{51}$$

where $x(k) \in \mathbb{R}^{n_x}$ denotes the state, $u(k) \in \mathbb{R}^{n_u}$ the control input, $y(k) \in \mathbb{R}^{n_y}$ the controlled output, and the scheduling parameter $\rho = \rho(k)$ is the real-time measurable rotor tilt angle during the transition flight. The LTI model between any two trimmed conditions can be deduced by linearly interpolating the adjacent LTI models obtained from the two trim solutions. For example, let $A(90)$ and $A(60)$ denote the A-matrix of two adjacent trimmed LTI models at tilt angle of 90° and 60°, respectively. Then, $A(p) = A(60) + \dfrac{p-60}{30}[A(90) - A(60)]$ for $p \in [60, 90]$.

In order to account for the equilibrium conditions defined in Eq. (39), the LPV model described in Eq. (51) must be extended as follows,

$$\begin{cases} x(k+1) = x_0(\rho) + A(\rho)x(k) + B(\rho)u(k) - [A(\rho)x_0(\rho) + B(\rho)u_0(\rho)] \\ \quad y(k) = y_0(\rho) + C(\rho)(x(k) - x_0(\rho)) \end{cases} \tag{52}$$

where the variables $x_0(\rho)$, $u_0(\rho)$, and $y_0(\rho)$ are linearly interpolated equilibrium conditions of the adjacent LTI models following the same method of interpolating the system matrices given earlier. For simplify, $x(k) - x_0(\rho)$ and $u(k) - u_0(\rho)$ in Eq. (52) are denoted as $\hat{x}(k)$ and $\hat{u}(k)$, respectively.

The adaptive MPC controller design [18–20] is to find the constrained control input $\hat{u}(k)$ that minimizes the constrained quadratic performance index, as formulated in the following,

Table 4
System input and output definitions.

System Input	Order	System Output	Order
Rudervator deflection	u_1	Rigid-body velocity	$y_{1:6}$
Rotor 3 tilt rate	u_2	Euler angle	$y_{7:9}$
Rotor 4 tilt rate	u_3	Body inertial position	$y_{10:12}$
Rotor spin acceleration	$u_{4:9}$	Rotor spin rate	$y_{13:18}$
		Angular position of rotor 3 and 4	$y_{19:20}$

Table 5
MPC controller spec parameters.

Parameter	Value	Parameter	Value
$Q_{[1,1]}$	1	$Q_{[2,2]}$	1
$Q_{[3,3]}$	500^2	$Q_{[4,4]}$	500^2
$Q_{[5,5]}$	1	$Q_{[6,6]}$	1
R	$0.1^2 \times I_9$		
Step Size	1 ms	Prediction Horizon	5 steps
min u_1	-0.1	max u_1	0.1
min $u_{[2,3]}$	$\frac{\pi}{2\times 45} - \varepsilon$	max $u_{[2,3]}$	$\frac{\pi}{2\times 45} + \varepsilon$
min $u_{[4:9]}$	0	max $u_{[4:9]}$	$\frac{P_{max}}{In_{[4:9]}(k)}$

$$\min_{u(0),\ldots,u(N_H-1)} \sum_{m=0}^{N_H-1} [\hat{x}^T(k+m)Q\hat{x}(k+m) + \hat{u}^T(k+m)R\hat{u}(k+m)] \quad \text{subject to} \quad G\hat{u}(k) \le h,\ k = 0, \ldots, N_H - 1 \tag{53}$$

where k denotes the current time step and N_H the finite horizon. The matrices $Q \ge 0$ and $R > 0$ are calibration weights used to penalize the state error and control effort, and G is the transmission matrix whose entries correspond to the input constraints. As a result, the optimization problem described in Eq. (53) can be reformulated as

$$\min_U \frac{1}{2}\left[U^T(k)(\hat{R} + \hat{B}^T\hat{Q}\hat{B})U(k) + \hat{x}^T(k)\hat{A}^T\hat{Q}\hat{B}U(k)\right] \quad \text{subject to} \quad \hat{G}U(k) \le \hat{h} \tag{54}$$

where $U(k) = [\hat{u}^T(k), \ldots, \hat{u}^T(k+N_H-1)]^T$ is the optimization vector, and $\hat{R}$, $\hat{B}$, $\hat{Q}$, $\hat{h}$, $\hat{A}$, and $\hat{G}$ depend on matrices Q, R, G, h in Eq. (53) and $A(\rho)$ and $B(\rho)$ in Eq. (51), and they are defined by

$$\begin{aligned}
&\hat{R} = block\ diag\left[R, R, \ldots, R\right] \in \mathbb{R}^{Nn_u \times Nn_u},\ \hat{Q} = block\ diag\left[Q, Q, \ldots, Q, 0\right] \in \mathbb{R}^{(N_H+1)n_x \times (N_H+1)n_x} \\
&\hat{G} = \begin{bmatrix} G & 0 & 0 \\ 0 & \ldots & 0 \\ 0 & 0 & G \\ 0 & 0 & 0 \end{bmatrix} \in \mathbb{R}^{(N_H+1)n_u \times (N)n_u},\ \hat{h} = \left[h^T, h^T, \ldots, h^T, 0\right]^T \in \mathbb{R}^{(N_H+1)n_u \times 1} \\
&\hat{A}^T = \left[I, A^T, \ldots, (A^T)^N\right] \in \mathbb{R}^{(N_H+1)n_x \times n_x},\ \hat{B} = \begin{bmatrix} 0 & 0 & \ldots & 0 \\ B(\rho) & & & \\ A(\rho)B(\rho) & B(\rho) & & \\ \ldots & \ldots & \ldots & \\ A^{(N-1)}(\rho)B(\rho) & A^{(N-2)}(\rho)B(\rho) & \ldots & B(\rho) \end{bmatrix} \in \mathbb{R}^{(N_H+1)n_x \times Nn_u}.
\end{aligned} \tag{55}$$

In real-time controller design, at current time k with given state $\hat{x}(k)$, the optimization problem described in Eq. (54) is solved using the QP (quadratic programming) solver in Matlab [22] and the solution $U(k) = [\hat{u}^T(k), \ldots, \hat{u}^T(k+N_H-1)]^T$. Then, $u = \hat{u}(k)$ will be used as the control input at current time step k. The optimization process is repeated for next time step $k+1$ and the control input $\hat{u}(k+1)$ can be solved accordingly [18–20].

6.2. Numerical simulation

Table 4 defines the list of inputs and outputs used in the simulations. To achieve the desired closed-loop system performance, the weighting matrices Q and R of Eq. (53) are chosen as in Table 5, where all undefined entries equal to zeros, in addition, the input constraints are also defined in Table 5. ε is chosen to be small enough, leading to a constant controlled mid rotor tilt rate. Note that u_4 to u_9 denote respectively the controlled spin acceleration for each rotor, with its upper bound computed based on the motor peak power P_{max}, where I and $n(k)$ denote the rotor inertia and speed, respectively;

To demonstrate the efficacy of the proposed LPV-based transition flight controllers, the closed-loop simulations are conducted by applying the proposed controllers to: 1) LPV LTI models presented in Eq. (52), and 2) nonlinear rigid-body flight dynamic model described in Eqs. (19), (21) and (24). Fig. 14 shows the proposed verification process for the transition flight controller, in which the red- and blue-dashed loops represent the LPV controllers closing the loop with LPV models and nonlinear rigid-body model, respectively. Furthermore,

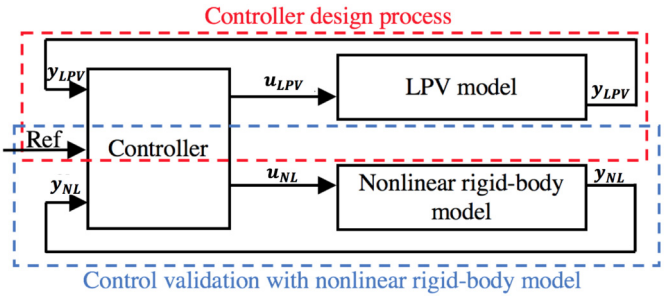

Fig. 14. Transition flight control verification process.

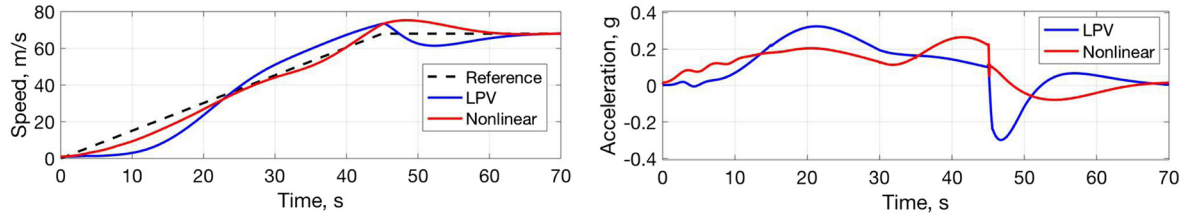

Fig. 15. Level flight speed and acceleration.

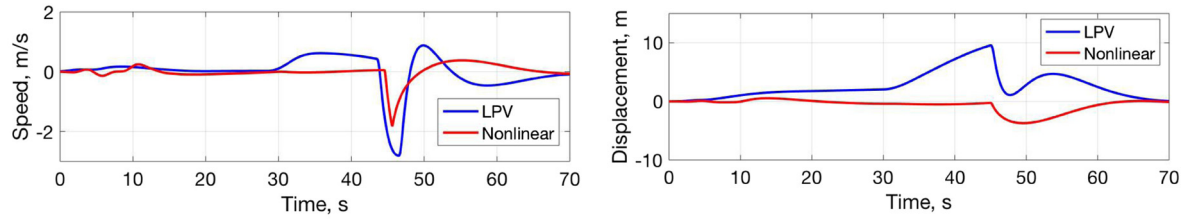

Fig. 16. Vertical speed and displacement.

it should be noted that the red-dashed loop is mainly used for calibrating the controller to achieve the desired closed-loop performance, while the blue-dashed loop is for validating the proposed transition flight controllers using the nonlinear aircraft model. In what follows, we present the simulation results by comparing y_{LPV} (LPV) and y_{NL} (Nonlinear) of Fig. 14.

The transition from hovering to forward flight is set to complete within 45 s, which roughly corresponds to a rotor tilt angular rate of 2 deg/s, and this number matches well with an earlier study in [2]. In the simulations, an additional 25 s is added to allow for the aircraft to converge to a stable level flight condition. Note that after 45 s, the control law is switched to an LTI controller that is designed based on the level flight model. Again, this level flight model is the trimmed model when the rotor tilt angle is set to 0°. The weighting for level flight speed $Q_{[2,2]}$ is chosen to be 200^2, this ensures the level flight speed to converge to the nominal speed of 68 m/s. In addition, the reference vertical speed v_z is chosen to be a function of altitude variation ΔH, i.e., $v_z = -0.3\Delta H$, in order to maintain the aircraft at the nominal altitude (304.8 m). Note that during the transition, the control strategy is developed based LPV model which could be more conservative than the one designed based on the LTI model. As a result, at the end of transition, it is desired to switch the control based on linearized LTI model.

Fig. 15 shows the level flight speed accelerating from 0 m/s to 68 m/s during the transition flight. However, both LPV and nonlinear models exhibit unwarranted overshoot when switching from transition flight to level flight at 45 s and beyond. This is attributed to the fact that switching between two flight control laws is prone to induce undesirable perturbation. In addition, when compared with the reference speed trajectory during the transition, the LPV models apparently yield a larger error. This is most likely caused by the linear interpolation of two trimmed models at two tilt angles that are too far apart. This modeling error can be reduced if the resolution of the tilt angle step size can be made smaller. However, this will result in a larger number of LPV models, hence a higher computational burden.

The vertical speed and displacement during the transition are shown in Fig. 16. Here, the desired vertical speed and displacement are zero. Again, we observe larger errors for LPV models, especially when transitioning from 45 s and beyond, which is precisely at the juncture of hovering and level flight. Furthermore, in Fig. 16, it should be noted that for both LPV models and nonlinear model, the large vertical speed drop after 45 s is again due to the control mode switch from the normal transition flight MPC to the final LTI level flight control. However, for both models, the final vertical speed and displacement are suppressed to zero.

Fig. 17 shows the aircraft pitch angle and pitch rate response during the transition flight. During the first 45 s of transition flight, the aircraft operates like a quadcopter, i.e., the aircraft pitches down to gain the longitudinal force components generated from the thrust vector of all rotors. This induces forward acceleration, as shown in Fig. 15. At 45 s, the aircraft starts to pitch up to decelerate so that the level flight speed can be reached at the nominal/equilibrium speed of 68 m/s, in the meantime, the lateral speed and roll and yaw rates are held at zero. The rotor rotational speeds are shown in Fig. 18, where the rotors are grouped as “front” (blue), “mid” (black), and “rear” (red), according to Fig. 7. All rotor speeds track the trimmed solution accurately and converge to the aircraft’s level flight equilibrium solution. Again, we observe a larger discrepancy between the LPV models and the nonlinear model beyond 45 s.

Last but not the least, to study the impact of number of linearized models to control performance, a new LPV-based controller was designed following the same procedure but with 10 LTI models along the transition profile (10-degree gap from 90 down to 0 degree).

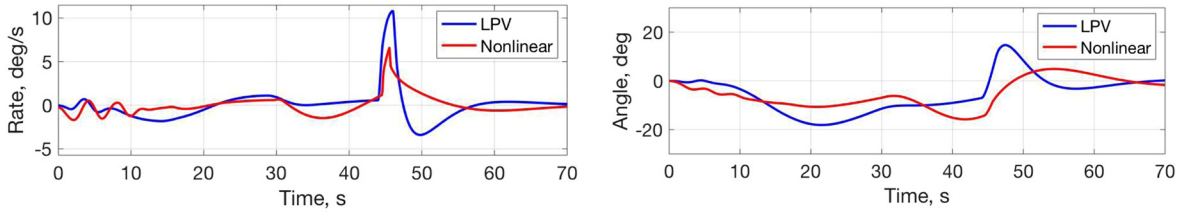

Fig. 17. Pitch rate and angle.

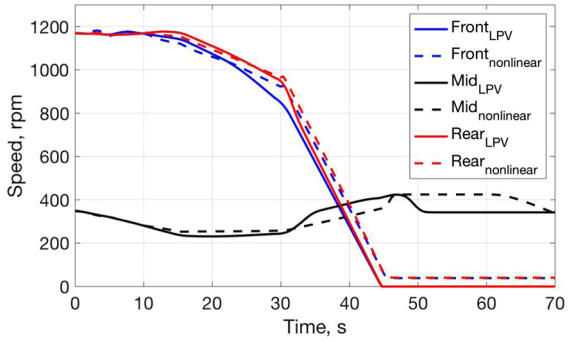

Fig. 18. Rotor rotational speed.

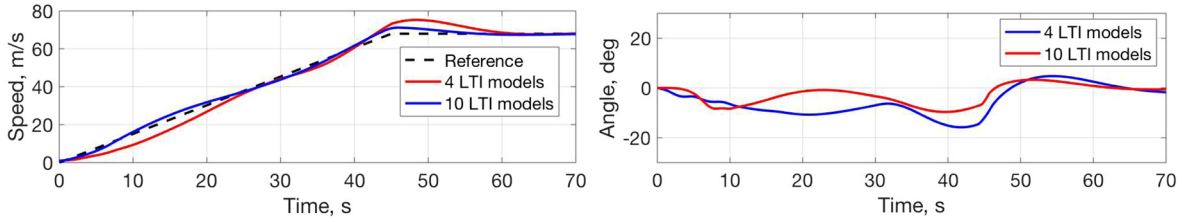

Fig. 19. Performance comparison of speed tracking and pitch angle.

The simulation is conducted based on the nonlinear rigid-body model, with the comparison of level flight speed tracking performance and pitch angle (see Fig. 19) The overall performance of the LPV model with increased number of linearized models is improved since it presents the original nonlinear model more accurately. The RMSE (root mean square error) of the speed tracking and pitch angle have been reduced from 3.66 to 1.57 and from 7.90 to 4.69, respectively. Note that the number of trimmed models used for LPV control design is related to how much memory used in the real-time controller, so it is desired to use minimal number of trimmed models with satisfactory performance. As discussed earlier, as the number of models increases, the closed-loop system performance improves. It is desired to select the smallest number of models when the performance no longer has significant improvement.

7. Conclusion

This paper presented an analytical approach for modeling aeromechanics and flight dynamics of tiltrotor eVTOL aircraft. Such hybrid vehicles have a fixed-wing platform configured with multiple tiltrotors on the wing members or fuselage. 6-DOF nonlinear rigid-body equations of motion were derived for the hybrid eVTOL aircraft, and the quaternions were used to describe the rigid-body kinematics. 2D potential flow-based aerodynamic loads were calculated over the lifting surfaces, the resultant lift and moment were then integrated into the complete vehicle's flight dynamics. Only the steady loads were considered in the current study. For simplicity, the rotor aerodynamic thrust and resistant torque were predicted using the Momentum Theory. This formulation captures the essential characteristics of rotor kinematics, such as tilt angle and spin rate, on the overall vehicle response and results in a highly nonlinear dynamic model. A comprehensive trim analysis was conducted at multiple flight conditions of interest, in which special attention was paid to the transition flight. A state-space LPV model was developed by considering the rotor tilt angle as the scheduling parameter. Finally, an adaptive MPC controller was designed based on the LPV models, and the closed-loop simulations demonstrated the effectiveness of the proposed transition flight control. A trade-off study between model accuracy and computational efficiency, as well as smooth switching of flight control laws with guaranteed performance, were identified as critically important for the stable operation of eVTOL vehicles. These subjects will be investigated in future research.

Declaration of competing interest

The authors declare the following financial interests/personal relationships which may be considered as potential competing interests: Weihua Su reports financial support was provided by DENSO International America Inc Southfield.

Acknowledgement

The authors of the University of Alabama and Michigan State University acknowledge the funding support provided by DENSO International America, Inc. The views expressed in this paper are those of the authors and do not reflect the official position of the sponsor.

References

[1] H.D. Kim, A.T. Perry, P.J. Ansell, A review of distributed electric propulsion concepts for air vehicle technology, in: AIAA Propulsion and Energy Forum, Cincinnati, OH, 2018.
[2] R.K. Mehra, R.K. Prasanth, S. Gopalaswamy, XV-15 tiltrotor flight control system design using model predictive control, in: 1998 IEEE Aerospace Conference, Snowmass, CO, 1998.
[3] M. Mattaboni, P. Masarati, G. Quaranta, P. Mantegazza, Multibody simulation of integrated tiltrotor flight mechanics, aeroelasticity and control, J. Guid. Control Dyn. 35 (5) (2012) 1391–1405, https://doi.org/10.2514/1.57309.
[4] H. Yeo, W. Johnson, Assessment of comprehensive analysis calculation of structural loads on rotors, in: American Helicopter Society 60th Annual Forum Proceedings, Baltimore, MD, 2004.
[5] M. Tugnoli, D. Montagnani, M. Syal, G. Droandi, A. Zanotti, Mid-fidelity approach to aerodynamic simulations of unconventional VTOL aircraft configurations, Aerosp. Sci. Technol. 115 (2021) 106804, https://doi.org/10.1016/j.ast.2021.106804.
[6] R.J. Higgins, G.N. Barakos, S. Shahpar, I. Tristanto, A computational fluid dynamic acoustic investigation of a tiltwing eVTOL concept aircraft, Aerosp. Sci. Technol. 111 (2021) 106571, https://doi.org/10.1016/j.ast.2021.106571.
[7] O.A. Bauchau, N.K. Kang, A multibody formulation for helicopter structural dynamic analysis, J. Am. Helicopter Soc. 38 (2) (1993) 3–14, https://doi.org/10.4050/JAHS.38.2.3.
[8] W. Johnson, Technology drivers in the development of CAMRAD II, in: American Helicopter Society Aeromechanics Specialist Meeting, San Francisco, CA, 1994.
[9] W. Johnson, Rotorcraft dynamics models for a comprehensive analysis, in: American Helicopter Society 54th Annual Forum Proceedings, American Helicopter Society, Washington, DC, 1998.
[10] A. Abhishek, A. Datta, I. Chopra, Prediction of UH-60A structural loads using multibody analysis and swashplate dynamics, in: American Helicopter Society 62nd Annual Forum Proceedings, American Helicopter Society, Phoenix, AZ, 2006.
[11] D.H. Hodges, H. Saberi, R.A. Ormiston, Development of nonlinear beam elements for rotorcraft comprehensive analyses, J. Am. Helicopter Soc. 52 (1) (2007) 36–48, https://doi.org/10.4050/JAHS.52.36.
[12] H. Saberi, M. Hasbun, J.Y. Hong, H. Yeo, R.A. Ormiston, Overview of RCAS capabilities, validations, and rotorcraft applications, in: American Helicopter Society 71st Annual Forum, Virginia Beach, VA, 2015.
[13] J.F. Tan, T.Y. Zhou, Y.M. Sun, G.N. Barakos, Numerical investigation of the aerodynamic interaction between a tiltrotor and a tandem rotor during shipboard operations, Aerosp. Sci. Technol. 87 (2019) 62–72, https://doi.org/10.1016/j.ast.2019.02.005.
[14] Z. Wang, Q. Wang, H. Yu, D. Duan, Z. Ding, J. Li, Trimming analysis method of quad tilt rotor based on aerodynamic interference model, J. Aircr. 58 (2) (2021) 253–265, https://doi.org/10.2514/1.C035943.
[15] Y. Yuan, D. Thomson, D. Anderson, Application of automatic differentiation for tilt-rotor aircraft flight dynamics analysis, J. Aircr. 57 (5) (2020) 985–990, https://doi.org/10.2514/1.C035811.
[16] R. Tóth, F. Felici, P.S.C. Heuberger, P.M.J. Van den Hof, Discrete time LPV I/O and state space representations, differences of behavior and pitfalls of interpolation, in: 2007 European Control Conference, ECC, IEEE, 2007, pp. 5418–5425.
[17] S. Snyder, P. Zhao, N. Hovakimyan, Adaptive control for linear parameter-varying systems with application to a VTOL aircraft, Aerosp. Sci. Technol. 112 (2021) 106621, https://doi.org/10.1016/j.ast.2021.106621.
[18] C.E. Garcia, D.M. Prett, M. Morari, Model predictive control: theory and practice—a survey, Automatica 25 (3) (1989) 335–348, https://doi.org/10.1016/0005-1098(89)90002-2.
[19] D.Q. Mayne, J.B. Rawlings, C.V. Rao, P.O. Scokaert, Constrained model predictive control: stability and optimality, Automatica 36 (6) (2000) 789–814, https://doi.org/10.1016/S0005-1098(99)00214-9.
[20] E.F. Camacho, C.B. Alba, Model Predictive Control, Springer Science & Business Media, 2013.
[21] W.B. Greer, C. Sultan, Infinite horizon model predictive control tracking application to helicopters, Aerosp. Sci. Technol. 98 (2020) 105675, https://doi.org/10.1016/j.ast.2020.105675.
[22] C. Schmid, L.T. Biegler, Quadratic programming methods for reduced Hessian SQP, Comput. Chem. Eng. 18 (9) (1994) 817–832, https://doi.org/10.1016/0098-1354(94)E0001-4.
[23] M.P. Merchant, L.S. Miller, Propeller performance measurement for low Reynolds number UAV applications, in: 44th AIAA Aerospace Sciences Meeting and Exhibit, Reno, NV, 2006.